ELSEVIER

Ultramicroscopy 80 (1999) 19–39

ultramicroscopy

www.elsevier.nl/locate/ultramic

Rare-earth oxides with fluorite-related structures: their systematic investigation using HREM images, image simulations and electron diffraction pattern simulations

C. López-Cartes[a], J.A. Pérez-Omil[a,*], J.M. Pintado[a], J.J. Calvino[a], Z.C. Kang[b], L. Eyring[b]

[a]*Departamento de Ciencia de los Materiales e Ingeniería Metalúrgica y Química Inorgánica, Facultad de Ciencias, Universidad de Cádiz, Apartado 40, Puerto Real, Cádiz 11510, Spain*

[b]*Department of Chemistry and Biochemistry, Arizona State University, Tempe, AZ 85287-1604, USA*

Received 28 September 1998; received in revised form 6 April 1999

Abstract

A complete set of non-equivalent kinematic electron diffraction patterns corresponding to the main zone axis orientations, $\langle 1\,0\,0\rangle_F$, $\langle 1\,1\,0\rangle_F$, $\langle 1\,1\,1\rangle_F$ and $\langle 1\,1\,2\rangle_F$ have been calculated for most members of the homologous series of binary anion-deficient, fluorite-related higher oxides of the rare earth elements, whose structures are currently resolved or postulated on the basis of the "fluorite-type module theory". From an analysis of this set, specific electron diffraction patterns which allow an unequivocal identification of each phase can be sorted out. A systematic approach, based on the use of these calculated patterns, to make a reliable phase identification for any sample that contains a mixture of these phases is presented and applied to interpret different experimental electron diffraction patterns. The detailed interpretation of a number of experimental HREM images recorded on a sample of praseodymium oxide using a match with calculated images is also illustrated. These results and procedures provide supplementary confirmation of the fluorite-type module theory to explain the structural features of the higher rare earth oxide phases and provide the background necessary to characterize these materials reliably.

Keywords: Higher rare earth oxides; HREM; Image simulation

1. Introduction

The structural investigation of the fluorite related and oxygen-deficient phases resulting from the reduction of the higher rare earth oxides has been the focus of intensive research [1,2]. Both theoretical and practical reasons could be argued to justify interest in this particular topic. The improved and more comprehensive knowledge concerning extended defects and non-stoichiometry in oxide phases which is reached with such studies informs the theoretical goal. From the point of view of applications, it suffices to recall that oxides of the rare earths, either pure or mixed with a transition or a second 4f element oxide [3–5] are major components of a wide variety of materials currently employed as catalysts, fast-ion oxygen conductors

* Corresponding author. Tel.: + 34-56-83-08-28; fax: + 34-56-83-49-24.

E-mail address: jose.perez-omil@uca.es (J.A. Pérez-Omil)

0304-3991/99/$ - see front matter
PII: S0304-3991(99)00067-4

or chemical sensors, among other uses. The function of the oxide in these materials stems from the chemical activity of reduced, oxygen-deficient phases which is intimately related to their structures.

In the course of this investigation electron microscopic techniques have been fruitfully exploited and have allowed access to relevant crystallographic information about some of these phases. Thus, on the basis of electron diffraction patterns (EDPs) the unit cell constants of the different members of the homologous series of Ce, Pr and Tb were estimated [6,7]. Likewise, a matching procedure between experimental and calculated HREM images was used to derive further details about the structure of some of these phases [8–11]. However, due to technical difficulties such as beam tilt information or the absence of kinematic diffraction, the reliability of the structural models generated using this approach was limited. The assumption that oxygen vacancies should occur in pairs also restricted the number of models proposed to explain the contrasts observed in the experimental HREM images, and seriously limited the possibilities of a successful search by image simulation.

In spite of some success in structure clarification using electron beam techniques, the achievements realized did not suffice to reach a complete structural determination of any of the phases. As a matter of fact, only recently have the structures of five members of the homologous oxide series been refined from neutron powder diffraction data by the Rietveld method [12–15]. These refinements demonstrated that the vacant oxygen sites occur as divacancies, especially in the vacancy rich region, but also as single vacancies in the oxygen-rich regions. The detailed analysis of the information generated by neutron diffraction studies indicated that the eight oxygen positions in a fluorite unit cell have an equal *a priori* probability to become vacant. Each of the possible ways vacancies can be accommodated in a fluorite-type unit cell are designated as modules necessary to model the structure. Any stable phase in the homologous series of binary oxides must contain an integral number of all the possible vacant oxygen sites. Interaction between the vacant oxygen sites within the fluorite matrix results in an ordered spatial arrangement of the oxygen vacancies. The deployment of the vacant oxygen sites observed experimentally have been rationalized [16–20] using a set of rules which constitute the fundamental structural principles underlying the family of higher oxides of the rare earths. This rationalization is called the fluorite-type module theory (F-TMT).

This provides an approach to understanding the compositions, R_nO_{2n-2m}, of the currently stablished phases in the homologous series of Ce, Pr and Tb oxides and the structures of those phases already determined by neutron diffraction. Moreover, and mostly important, the F-TMT theory also enables a prediction of the structure of other reduced oxides in these series, whose existence is known from tensimetric studies and their lattice parameters estimated by electron diffraction, but which still await a definite refinement by neutron diffraction or other means.

The establishment of these structural foundations opens new possibilities for electron microscopic investigation of these and possibly other oxides, particularly for high-resolution electron microscopy. Thus, using adequate modeling tools like those provided by the RHODIUS software package developed at UCA [21], the unit cells corresponding to any member of the homologous series can be built up and, therefore, its behavior in a particular electron microscope characterized. With calculated EDPs and calculated HREM images available, the nanostructural characterization of materials based on rare earth oxides, like those cited in the previous paragraph, can be accomplished. Such studies should unveil the details necessary to understand the correlation between their structure and the macroscopic properties. Moreover, because of the stable face centered cubic array of the metal atom substructure, it is not difficult to envisage samples where microdomains of different composition and crystallography coexist within the same microcrystal. In such cases, electron microscopic techniques will be unique to provide the localized information required to describe precisely the nature of this texture.

In this contribution, a systematic investigation, by simulation, of some of the reduced phases whose structures are currently known or postulated has been carried out. EDPs corresponding to the main

zone axis of each phase have been calculated and compiled in the form of a phase-orientation atlas. From the analysis of the whole set of EDPs contained in this atlas, those orientations which allow an unambiguous identification of each phase can be determined. These characteristic EDPs can be used as fingerprints of a given phase, hence constitute extremely useful information when a complex sample containing a mixture of structures including polymorphs is being analyzed. From the discussion of this atlas, those particular orientations whose images require a detailed analysis by image simulation, in order to avoid misinterpretations, can also be identified. The interpretation of a series of experimental EDPs and digital diffraction patterns (DDPs) corresponding to HREM images recorded on a sample of praseodymium oxide partially reduced is accomplished to show, by example, how the phase-orientation atlas can be exploited.

A central point addressed in this paper is the possibility of matching the contrasts observed in experimental images with those calculated for particular structural models. The results obtained could test the validity of the F-TMT.

2. Experimental procedure

The EDPs and HREM images presented in this paper correspond to samples of praseodymium oxide. Sample preparation and activation procedures have been described elsewhere [22]. This information was recorded using a JEOL4000-EX microscope operating at 400 kV. The electron optical parameter values of this equipment used as input for the calculation routines have been gathered in Table 1.

The simulations of electron diffraction patterns and HREM images have been done using different routines of the 3.3 version of the EMS package [23] running on an INDY4400SC SG Workstation. The unit cells employed as starting models for these simulations have been built using Fortran-coded routines developed at the University of Cadiz (UCA) for this specific purpose. The UCA programs allow calculation of the unit cell parameters and fractional coordinates of the asymmetric unit for any reduced R_nO_{2n-2m} phase, starting from the modular sequence description proposed in the original papers describing the F-TMT [16–20]. In these calculations the dimensions of the modules have been taken as those of the corresponding dioxide and the coordinates of the rare earth element within the modules as those in the ideal fluorite cell.

Table 1
Values of the electronoptical parameters employed for simulations microscope JEOL4000EX

HV[a] (kV)	Ap[b] (nm^{-1})	Cs[c] (mm)	Δ[d] (nm)	θ[e] (mrad)
400	13	1.0	8.0	0.6

[a] Operating voltage.
[b] Aperture diameter (in reciprocal space units).
[c] Objective lens spherical aberration coefficient.
[d] Defocus spread.
[e] Electron beam semiconvergence angle.

For the calculation of electron diffraction patterns kinematic conditions have been assumed. In the case of HREM images, dynamic diffraction and a non linear imaging process have been considered. The supercells employed for HREM image simulation have been generated using the RHODIUS programs [21] also developed at UCA. The slicing of these supercells was adjusted to maintain valid the basic assumptions of the multislice routines of EMS. No slices thicker than 2 Å were used. The dimensions of the supercells were selected, within the limits imposed by the specific crystallography of the corresponding phase, so as to obtain acceptable computing times using 512×512 or 1024×1024 samplings of the projected slice potentials. Image processing has been performed using the DOS version of the SEMPER6 + by Synoptics. Digital diffraction patterns (DDPs) were calculated using this software as the Fourier transform of the two-dimensional intensity distribution of images digitized using a conventional CCD camera.

Given that the structures of the reduced phases are related to that of fluorite, two different sets of indices can be used when naming a particular direction in direct or reciprocal space. Throughout the paper the subscript "F" will be used to refer to the fluorite set of axis, whereas, a Greek symbol subscript will be used to specify the crystal axis system.

Very simple crystallographic transformations relate both sets.

3. Results

In Table 2 a list of the different intermediate phases currently established in the homologous series R_nO_{2n-2m} can be found. The corresponding values of the phase designations, "n" and "m" in the generic formula and the composition are tabulated, so that henceforth these parameters will designate a particular phase. Two more columns indicating the crystal system in which each phase crystallizes and the current state of their study using neutron diffraction have also been added. Note that both phases whose structures have been determined by neutron diffraction and those that are predicted on the basis of tensimetric and electron microscopy investigations have been considered.

3.1. A systematic approach to the interpretation of the EDPs of R_nO_{2n-2m} phases: need and strategy

To introduce the basic features of the recorded EDPs of the homologous series of rare earth oxides, Fig. 1(a) shows an experimental EDP recorded from a praseodymium oxide sample. It is clearly seen that these patterns contain a series of high intensity spots and additional commensurate extra spots in between. The former arise from the parent fluorite substructure which is common to all members of the homologous series, as stated previously. In this particular case the high intensity spots can be properly indexed on the basis of a $[1\,1\,2]_F$ zone axis (where F stands for fluorite). The extra spots contain information about the superstructure which is generated as a consequence of the ordered arrangement of oxygen vacancies within the fluorite matrix. The number of superlattice reflections which can be counted in these $[1\,1\,2]_F$ zone axis patterns is related to the value of n in the generic formula of the homologous series, R_nO_{2n-2m}. Using the very simple rules that follow, which can be derived from the analysis of the crystallographic information obtained by F-TMT [16–20], such determinations can be easily carried out:

1. For those phases that show superlattice reflections aligned with those of the fluorite subcell along two different reciprocal directions, n corresponds to the total number of spots included within the reciprocal unit cell defined by the basic $(1\,1\,\bar{1})$ and $(2\,\bar{2}\,0)$ $\boldsymbol{g}$ vectors. For these phases monoclinic unit cells can be defined.
2. In those cases where alignment between fluorite and superlattice spots is restricted to one reciprocal direction, the value of n can be directly determined by counting the number of intervals between two neighboring fluorite reflections. For these phases crystallization occurs in non-monoclinic unit cells.

The EDP of Fig. 1(a) falls into the first category. A total of 24 reflections can be counted in the dashed rectangle shown, and this allows us to assign this diffraction pattern to the composition $Pr_{24}O_{44}$. For this composition the expected structure is $\beta(1)$, Table 2. To confirm this assignment the unit cell of this phase was constructed and the EDPs corresponding to the 12 zone axes resulting from the crystallographic transformation of the $\langle 1\,1\,2\rangle_F$-type zones calculated. It should be mentioned that although in the fluorite cell itself all the $\langle 1\,1\,2\rangle$ axes are equivalent, this is not true for the $\beta(1)$ because of its lower spatial symmetry. From the entire set of simulated EDPs shown in Fig. 2, which corresponds to the zone axis $[1\,1\,2]_F$, the only one matching that in Fig. 1(a) was that from the $[1\,0\,0]_{\beta(1)}$ zone. Moreover, and perhaps the most important, this result indicates that on the basis of the models built using the F-TMT, the geometry and superlattice features of EDPs like this can be thoroughly explained. Further dynamic calculations should be undertaken in order to reproduce more closely, in the calculated pattern, the distribution of diffracted intensity observed in the experimental one. In such case the effect of crystal thickness, crystal tilt and most important, the relaxation of atoms in the surroundings of the oxygen vacancies, with respect to the positions in an ideal fluorite structure, should be taken into account.

All the phases listed in Table 2 present at least one EDP along a specific $\langle 1\,1\,2\rangle_F$ zone axis where the complete superstructure is revealed. On the

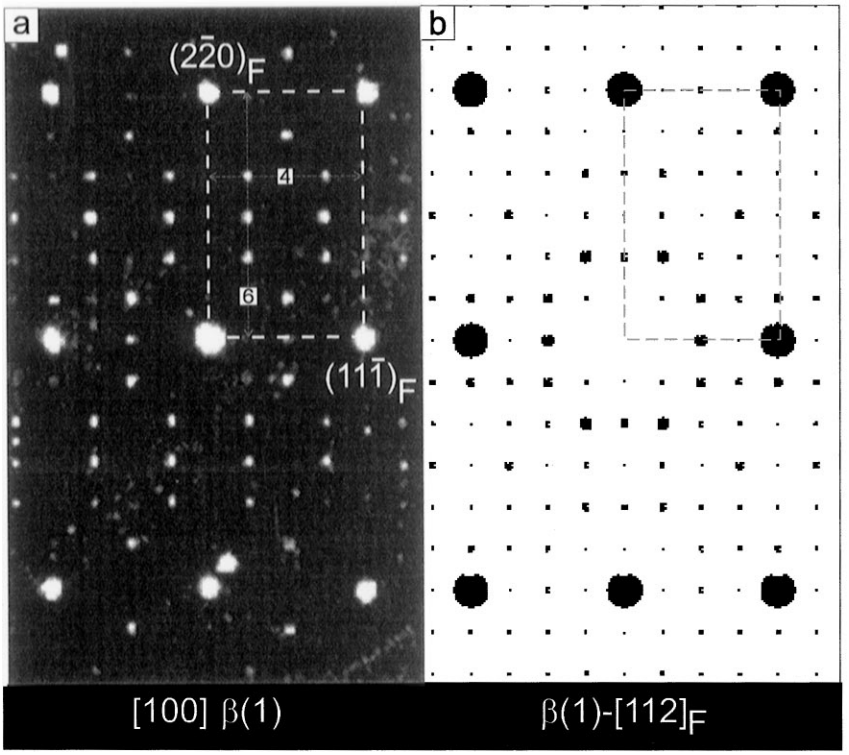

Fig. 1. Experimental (a) and simulated EDP (b) of the $\beta(1)$-phase along $[1\,1\,2]_F$.

Table 2
Known phases in the homologous series R_nO_{2n-2m}

Phase	n	m	Formula		Crystal system	Neutron diff.
ι	7	1	R_7O_{12}	($RO_{1.714}$)	Rhomboedral	Yes
ζ	9	1	R_9O_{16}	($RO_{1.778}$)	Triclinic	Yes
δ(1)	11	1	$R_{11}O_{20}$	($RO_{1.818}$)	Triclinic	Yes
π	16	1	$R_{16}O_{30}$	($RO_{1.875}$)	Undetermined	No
M19	19	2	$R_{19}O_{34}$	($RO_{1.789}$)	Triclinic	No
β(1)	24	2	$R_{24}O_{44}$	($RO_{1.833}$)	Monoclinic	Yes
β(2)	24	2	$R_{24}O_{44}$	($RO_{1.833}$)	Undetermined	No
M29	29	3	$R_{29}O_{52}$	($RO_{1.793}$)	Undetermined	No
M39	39	4	$R_{39}O_{70}$	($RO_{1.795}$)	Undetermined	No
ε	40	4	$R_{40}O_{72}$	($RO_{1.800}$)	Monoclinic	Yes
β(3)	48	4	$R_{48}O_{88}$	($RO_{1.833}$)	Undetermined	No
δ′	62	6	$R_{62}O_{112}$	($RO_{1.806}$)	Undetermined	No
δ(2)	88	8	$R_{88}O_{160}$	($RO_{1.818}$)	Undetermined	No

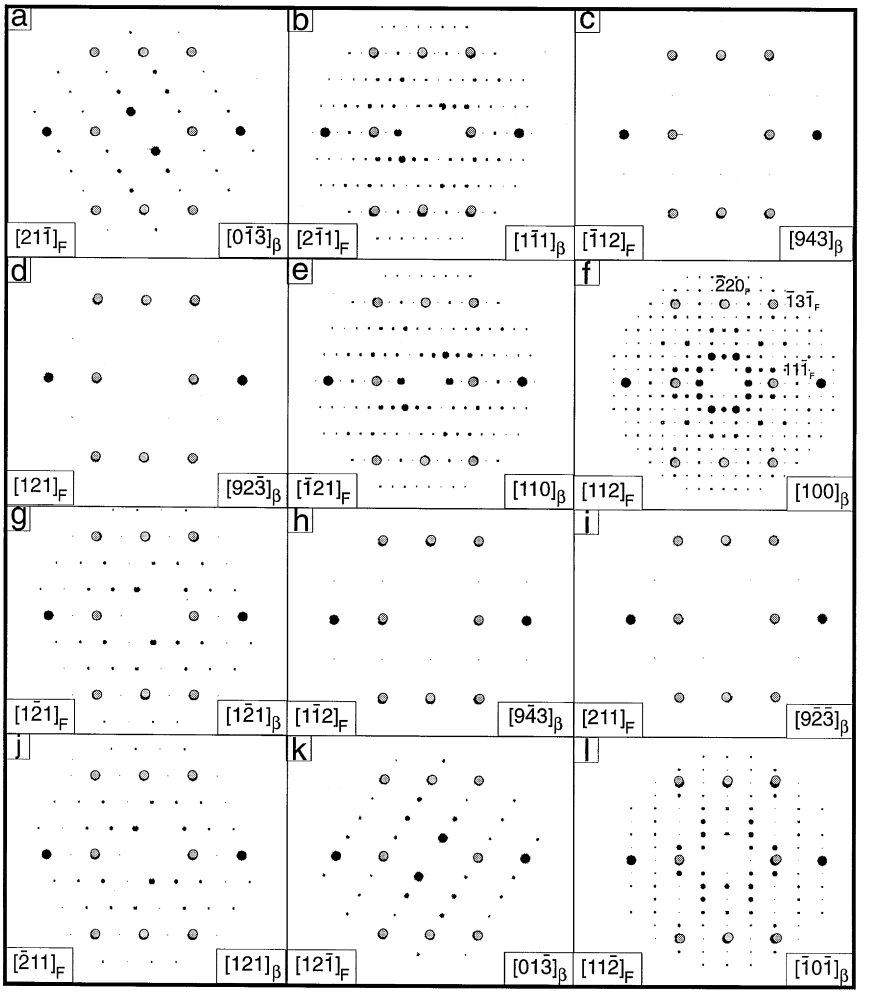

Fig. 2. Simulated EDPs of the $\beta(1)$-phase in the $\langle 1\,1\,2\rangle_F$ orientation.

basis of this unique $\langle 1\,1\,2\rangle_F$ pattern a successful identification of any phase is possible. Which ones of the 12 $\langle 1\,1\,2\rangle_F$ axes will satisfy this requirement depends on the precise relationships that are established between the fluorite and the superstructure crystal axes in each particular phase. To clarify this point, Fig. 2 shows the complete set of calculated EDPs for the $\beta(1)$ phase which come from the transformation of the 12 $\langle 1\,1\,2\rangle$ fluorite orientations. It can be observed that although in any of them the high intensity fluorite spots are identical, the number and arrangement of superlattice spots vary significantly. Thus, for the $[\bar{1}\,1\,2]_F$, $[1\,2\,1]_F$, $[1\,\bar{1}\,2]_F$ and $[2\,1\,1]_F$ zone axes (patterns c, d, h and i, respectively), no extra spots of significant intensity are evident. Likewise, for others like those in Fig. 2(a), (b), (e), (g), (j), (k) or (l), the number of superlattice spots is much lower than 24. These patterns cannot lead to a misleading phase assignment because the corresponding n numbers that are obtained from them are, in all cases, lower than 7, which is the least value (Table 2) for this parameter. Only the EDP corresponding to the $[1\,1\,2]_F$ zone axis, 2(f), would be suitable to establish the value of n, as previously mentioned.

Pattern $[1\,1\,\bar{2}]_F$, Fig. 2(l) needs further comment. Fig. 2(l) shows that the superstructure spots along $[2\,\bar{2}\,0]$ are the same as in Fig. 2(f), but there are only two rows of spots along $[1\,1\,\bar{1}]$ instead of four as in Fig. 2(f), therefore, the unit cell in this orientation is just half the true unit cell. Actually, the two vacant oxygen sites are eclipsed in the $[1\,1\,\bar{2}]$ orientation of $\beta(1)$ making the unit cell appear to be half its true value. One might mistake this for an $n = 12$ phase, for which a $\beta(0)$ phase had been previously proposed.

This particular example points out the convenience of creating a complete set of calculated EDPs for all the phases. From the analysis of such a set, both patterns which are strictly specific to one phase and those which could be interpreted as due to more than one phase can be sorted out. With this information in hand, phase identification in materials containing these oxides would certainly be a faster task and, definitely, more reliable.

3.2. EDP atlas

Accepting this approach, the complete set of EDPs for some members of the homologous series included in Table 2 have been calculated along the following main, low index zone axes: $\langle 1\,0\,0\rangle_F$, $\langle 1\,1\,0\rangle_F$, $\langle 1\,1\,1\rangle_F$ and $\langle 1\,1\,2\rangle_F$. Given that the f.c.c.

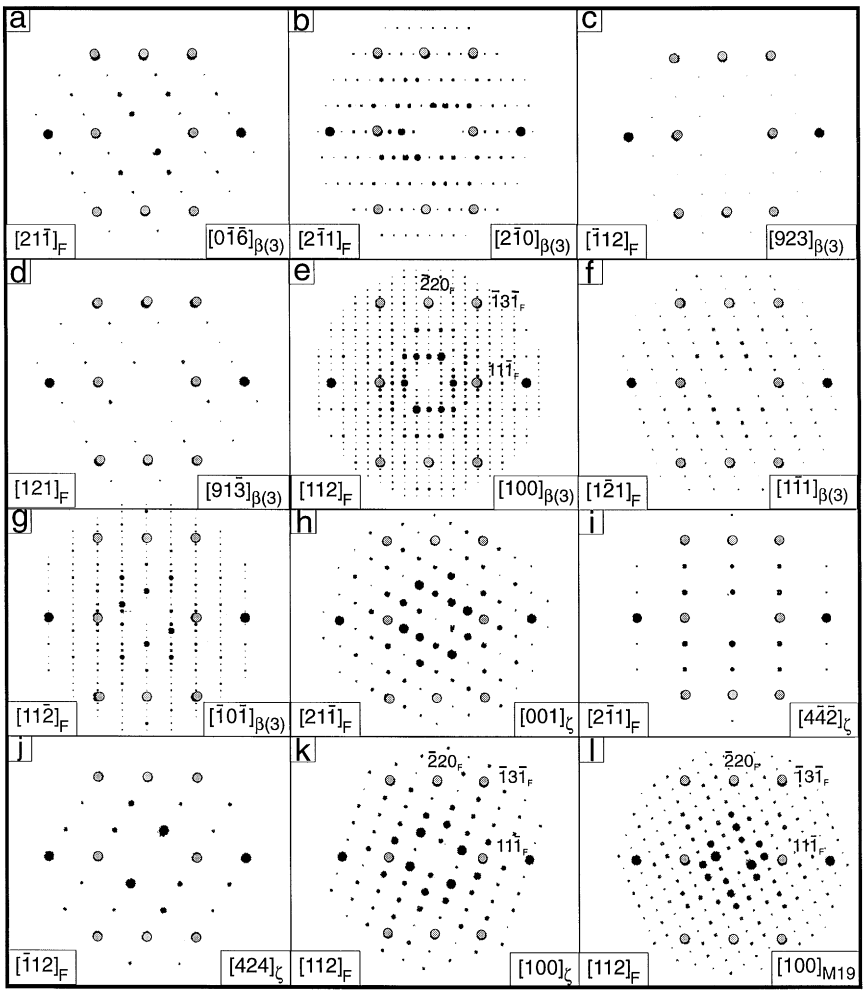

Fig. 3. Simulated $\langle 1\,1\,2\rangle_F$ EDPs of selected reduced rare earth oxide phases.

symmetry is lost in the reduced phases all the components of each zone axis type have been considered. For example $[0\,0\,1]_F$, $[0\,1\,0]_F$ and $[1\,0\,0]_F$ patterns have been obtained for each phase. Likewise six and 12 directions were considered for the $\langle 1\,1\,0\rangle_F$ and $\langle 1\,1\,2\rangle_F$ directions, respectively. Figs. 3–6 show the results of these calculations. This compilation of EDPs constitutes the basic background needed for the interpretation of both experimental EDPs and calculated DDPs following the procedure outlined below. Before going into this, some ideas related to the analysis of these figures should be mentioned.

A point of interest is the absence of superlattice spots for certain orientations and phases. Thus, in the case of the δ-phase only two from the 12 possible $\langle 1\,1\,2\rangle_F$-type orientations show superstructure reflections, Fig. 3(n) and (o). The calculated EDPs obtained for the remaining ten contain only the spots from the fluorite subcell. Extreme cases in this respect are also the M(19) phase for which only one $\langle 1\,1\,2\rangle_F$ pattern, that of $[100]_{M(19)}$, exhibits superlattice spots. None of the six $\langle 1\,1\,0\rangle_F$ EDPs for ι, δ, or M19 show superlattice reflections These EDPs and, consequently, the HREM images that could be obtained from such zone axes will contain no information about the superstructure and, therefore, could be incorrectly assigned to a non-reduced material. To avoid such a mistake, the interpretation of more than one zone axis pattern from the same crystal region would be necessary. From an analysis of the EDP atlas presented here, convenient EDP zone axis combinations can be selected, as required for the unequivocal identification of a phase.

A second question that must be addressed is related to the possibility of multiple assignments for a given pattern. In effect, it can be observed that there are a number of EDPs, corresponding to different phases, that are identical. This is the case, for example, of the EDPs calculated for $[0\,\bar{1}\,\bar{6}]_{\beta(3)}$, Fig. 3(a), which cannot be

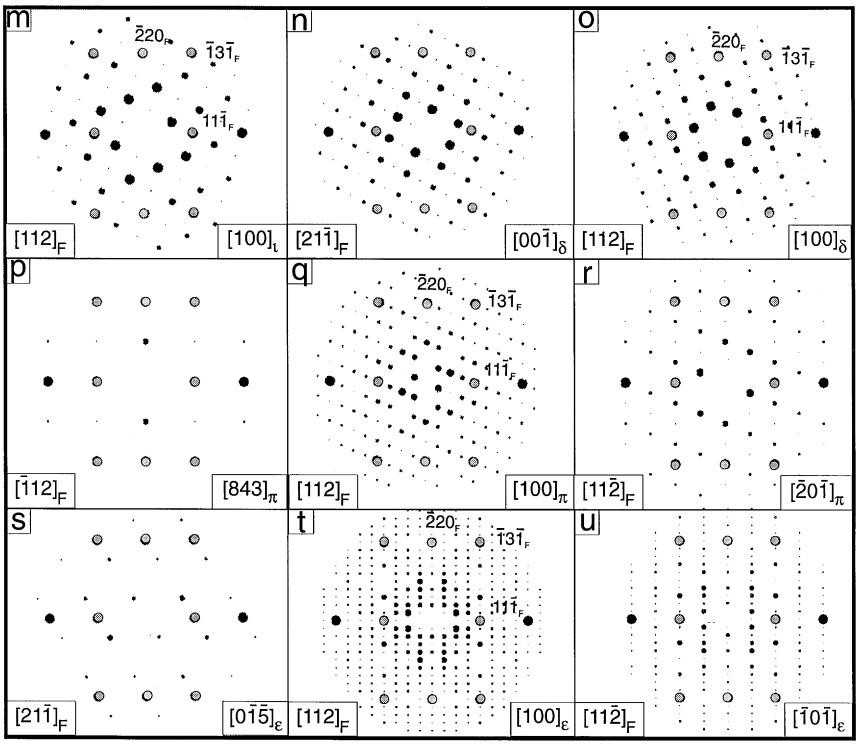

Fig. 3. Continued.

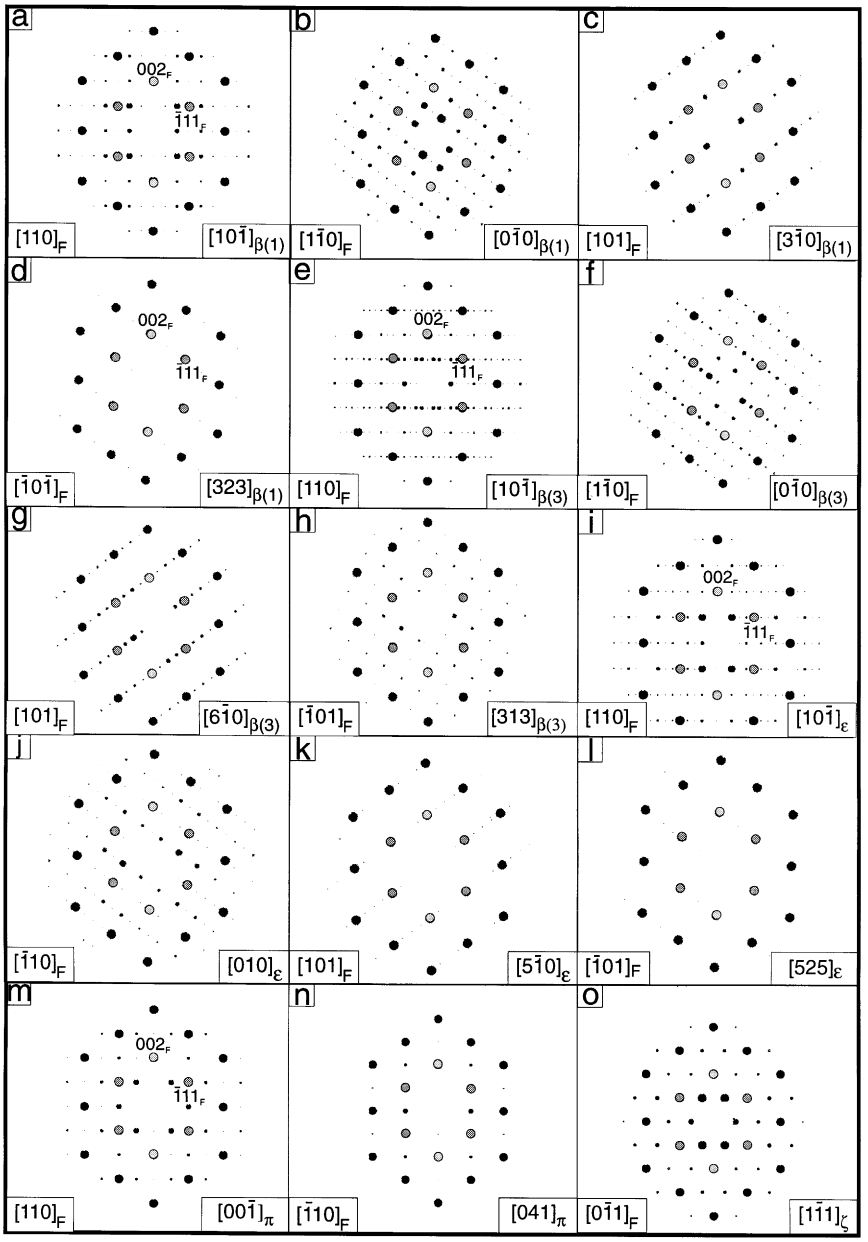

Fig. 4. Simulated $\langle 1\,1\,0\rangle_F$ EDPs of selected reduced rare earth oxide phases.

distinguished from those of $[0\,\bar{1}\,\bar{3}]_{\beta(1)}$, Fig. 2(a), or $[0\,\bar{1}\,\bar{5}]_{\varepsilon}$, Fig. 3(s). From the point of view of the number and position of superlattice spots all these EDPs are equivalent. However, the dynamic scattering can change the intensity distribution and their intensities may be different. Although this particular point will not be developed here, it is clear that from the exhaustive analysis of

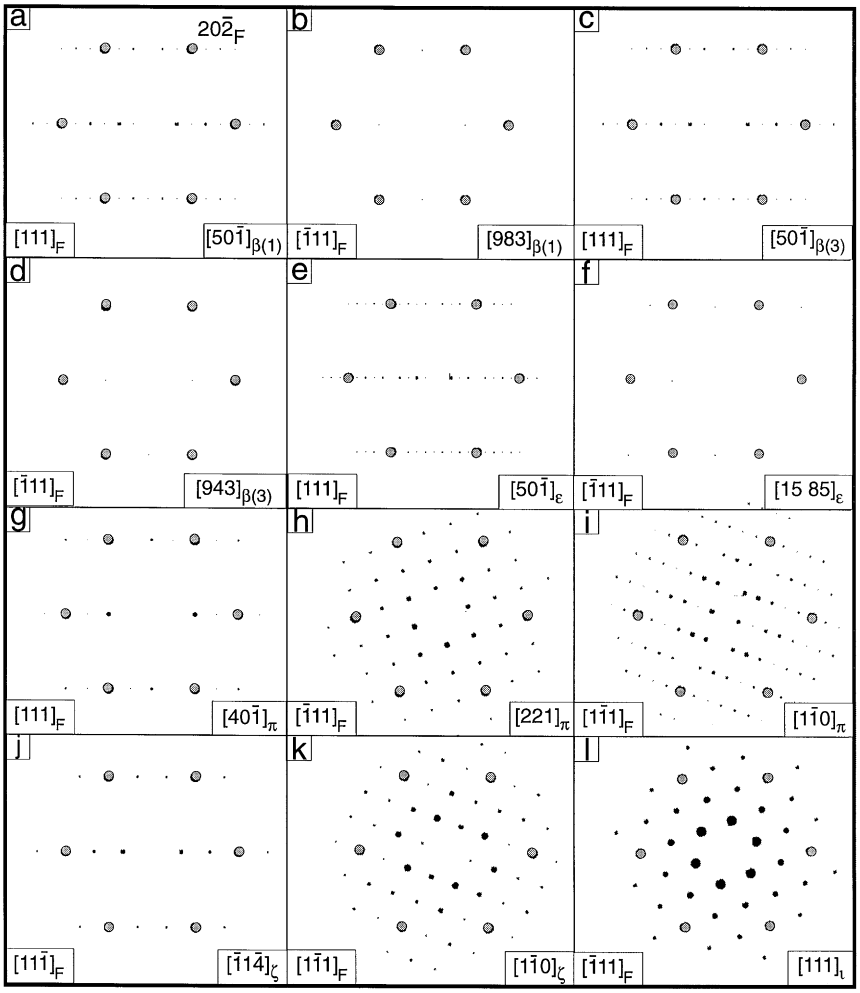

Fig. 5. Simulated $\langle 1\ 1\ 1\rangle_F$ EDPs of selected reduced rare earth oxide phases.

the whole set of calculated EDPs it would be possible to sort out all the sets of equivalent EDPs.

Finally, it is important to stress that the atlas calculated in this work not only provides a global view of the EDPs in this family of oxides, which is certainly of intrinsic interest, but also warns of problems that may arise during their interpretation and allows strategies to circumvent them to be defined.

3.3. Interpretation of specific examples

In this section several experimental EDPs will be interpreted and assigned to particular reduced phases using the information provided by the calculated EDP atlas. The first EDP, recorded on a praseodymium oxide sample, is shown in Fig. 7(a). In this case the basic $[1\ 1\ 2]_F$ substructure can be clearly identified. On the other hand, the superlattice framework is characterized by eight

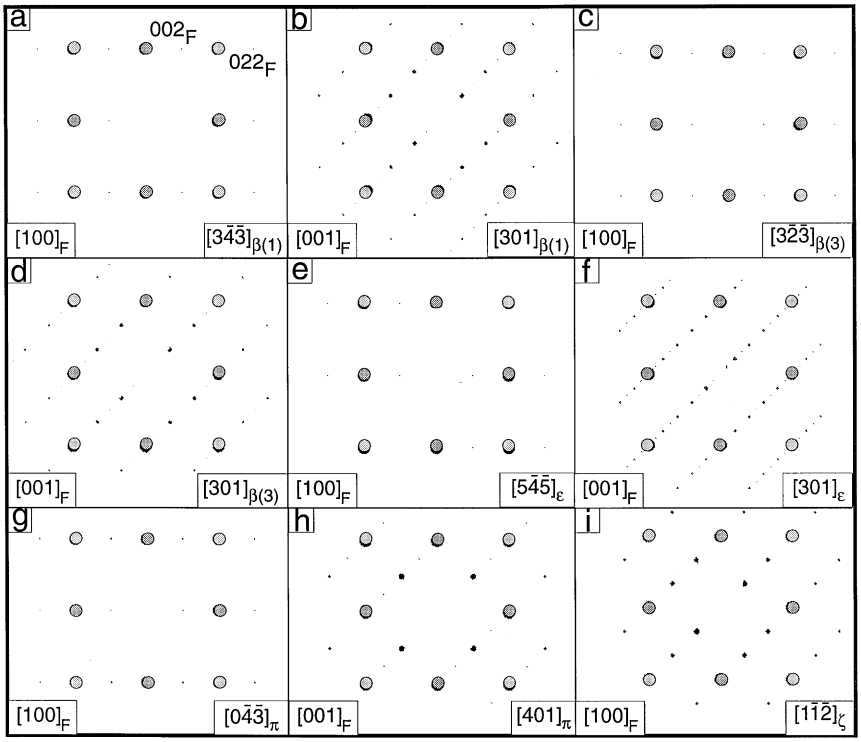

Fig. 6. Simulated $\langle 1\,0\,0\rangle_F$ EDPs of selected reduced rare earth oxide phases.

superstructure spots between the fluorite spots along the $[\bar{3}\,5\,\bar{1}]_F$ reciprocal direction. After reviewing the entire collection of $\langle 1\,1\,2\rangle_F$ patterns, the only one which presents this feature is that corresponding to $[1\,0\,0]_\zeta$, Fig. 3(k). This pattern, which corresponds to a phase whose structure is established by neutron diffraction, is completely specific for this phase in this particular orientation, which makes this interpretation reliable without the need for further work.

The EDP shown in Fig. 7(b) provides an example of patterns recorded along a $\langle 1\,1\,0\rangle_F$ direction. A total of five superlattice spots are observed in this case aligned with the fluorite reflections along the $\langle 2\,2\,0\rangle_F$ reciprocal direction. The calculated pattern corresponding to $[1\,0\,\bar{1}]_{\beta(1)}$ is the only one that matches the experimental one, Fig. 4(a). Therefore, an unambiguous conclusion about the phase giving rise to this pattern can also be reached.

Finally, Fig. 7(c) allows interpretation of an EDP pattern recorded along a $\langle 1\,1\,1\rangle_F$ direction. From the whole set of calculations corresponding to this fluorite orientation, the simulated pattern corresponding to $[1\,\bar{1}\,0]_\zeta$ Fig. 5(k) is the only one that explains the observed superlattice features.

In the past a diffraction pattern identical to that shown as Fig. 3f, $[1\,\bar{1}\,1]_{\beta(3)}$ was assigned as due to a phase $\beta(0)$ along $[1\,0\,0]_{\beta(0)}$, a primitive unit cell in the series $R_nO_{2n} - 2_m$ with two vacancies, where $n = 12$ and $m = 1$. This cell would belong to a subgroup with $n = 7$, 9, 11, and 16. A second selected area diffraction pattern from the same crystal having a common axis was not obtained to establish the unit cell. It is, nevertheless, possible to decide whether the pattern could be from such a $\beta(0)$-phase by examining the pattern for diffraction spots arising from a higher-order Laue zone (HOLZ). The intermediate anion-deficient, fluorite-related oxide unit cells usually have one short axis and two longer ones. If the pattern comes from an orientation along a short axis the HOLZ pattern will be relatively far from the zero-order

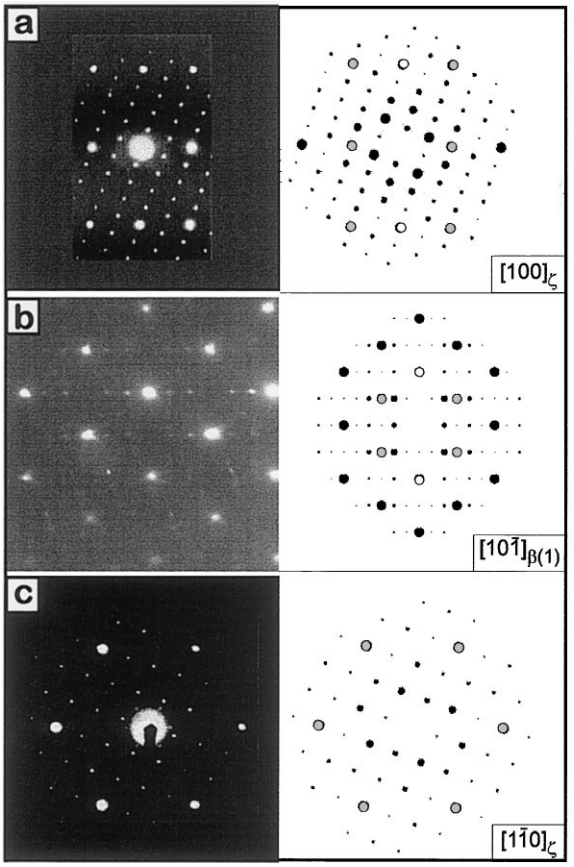

Fig. 7. EDPs and calculated diffraction patterns of ζ and $\beta(1)$-phase.

Laue zone (ZOLZ) pattern and there will not be any overlap of spots. However, if the pattern is from along a higher-index zone direction there could be an overlap [24]. The pattern that prompted assignment of a $\beta(0)$ phase shows some overlap of spots from the HOLZ pattern, hence, it must not be from the $[1\,0\,0]_{\beta(0)}$ phase but is more likely from the higher-index zone $[1\,\bar{1}\,1]_{\beta(3)}$.

The main conclusion that should be drawn from this section is that the different examples treated clearly indicate that the unit cells generated on the basis of the F-TMT for this family of oxides, explains the details observed in experimental EDPs. Hence, these results provide further support to the model. DDPs obtained from HREM images can be also fruitfully interpreted, as will be shown below using the same procedures.

3.4. HREM images

Different aspects related to the interpretation of HREM images will be dealt with in the remainder of this paper. Fig. 8 contains an experimental HREM image of a praseodymium oxide sample. In the corresponding DDP, inset in the figure, the basic $[1\,\bar{1}\,0]_F$ spots are present. Rather intense additional superlattice spots are also observed between the fluorite ones, three along the $[1\,1\,3]_F$ reciprocal direction and one along the $[\bar{1}\,\bar{1}\,1]_F$ direction.

A search in the collection of diffraction patterns indicates that this image could correspond, to the [0 1 0]-type orientation of any of the following reduced phases: $\beta(1)$, $\beta(3)$ or ε. In these three cases, the calculated diffraction patterns, Fig. 4(b), (f) and (j), indicate the presence of three extra spots along both $[1\,1\,3]_F$. The only distinguishing feature is the relative intensities of the superlattice spots along

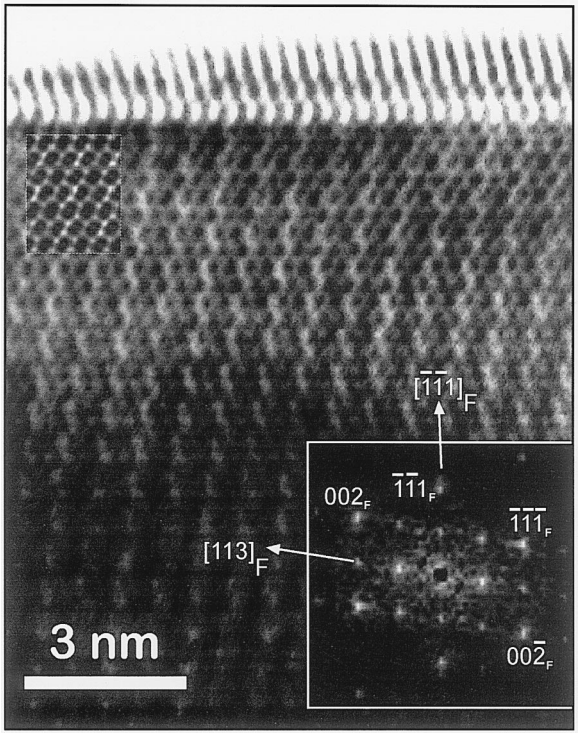

Fig. 8. Experimental image of a region of $\beta(1)$-phase with simulation and DDP insets.

$[\bar{1}\,\bar{1}\,1]$. According to dynamic calculations performed for the $\beta(1)$ phase, from the three superlattice spots that lie along $[\bar{1}\,\bar{1}\,1]_F$, the one just at the center between the fluorite spots is the most intense whereas those at $\frac{1}{4}$th and $\frac{3}{4}$th present a negligible intensity in the 0–100 nm thickness range. For the $\beta(3)$ dynamic calculations, a significant and comparable intensity is found for these three spots. In contrast, for the epsilon phase, calculations show a very small intensity for the three extra spots along $[1\,1\,3]_F$, those at the center being the least intense. Though the relative intensities of these reflections could change in the imaging step, these calculations suggest that the experimental image in Fig. 8 could correspond to $[0\,1\,0]_{\beta(1)}$. Given that the other two possibilities cannot be ruled just on the basis of EDPs calculated under dynamic diffraction conditions, to confirm this hypothesis models of $\beta(1)$, $\beta(3)$ and ε in $[0\,1\,0]$, considering crystals of increasing thickness, were built using the RHODIUS program. From these models calculated images and their corresponding DDPs were obtained. Fig. 9 shows the result of these calculations, considering the electron optical parameters of a JEOL-4000EX (Table 1), for the $\beta(1)$ phase. Note that the image corresponding to the calculation for the 15 nm-thick crystal at -10 nm defocus shows a fairly good match with the experimental image. Thus, the low-frequency contrast modulation, commensurate with the fluorite structure, which is clearly observed along the $[1\,1\,3]_F$ direction of the experimental image is reproduced in the calculation. A portion of this simulated image has been inset in the experimental

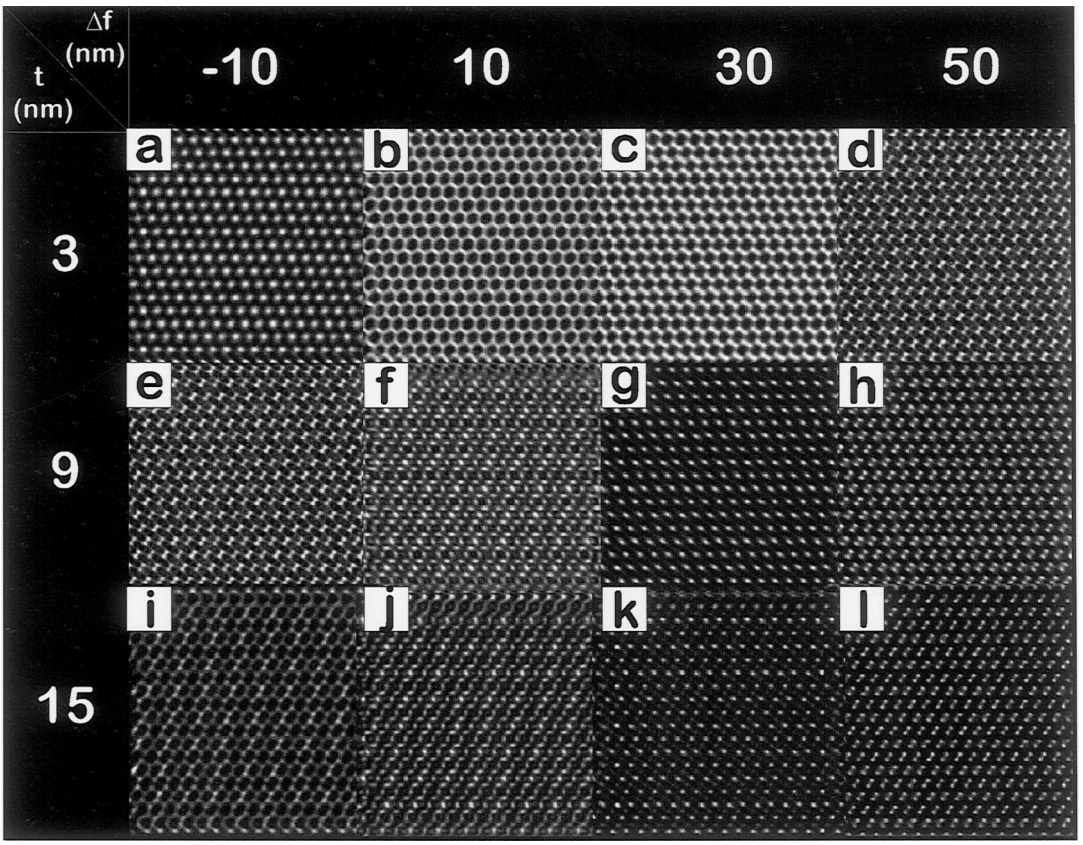

Fig. 9. Simulation of images of $\beta(1)$-phase in the $[\bar{1}\,1\,0]_F$ zone according to thickness and defocus.

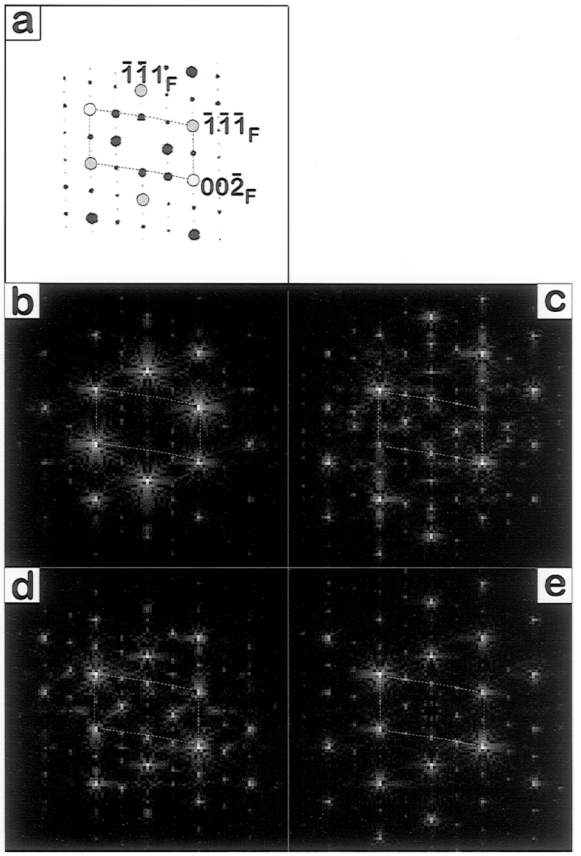

Fig. 10. Comparisons between the DDP from the image shown in Fig. 8 and those calculated for β(1)-phase.

image for comparison. The DDP corresponding to this calculated image, Fig. 10(c) agrees very well with that of the experimental image and contains the superlattice spots in the correct number and positions. Note that the spots at $[\bar{1}\ \bar{1}\ 1]_F$ are rather intense. Fig. 11(a) and (c) show the images calculated for 15 nm thick crystals of β(3) and ε, respectively. Although the modulation contrasts are also visible in these images they seem not to provide as good a fit to the experimental HREM image, specially in the case of the epsilon phase. A similar conclusion is obtained from a comparison of their DDP, Fig. 11(b) and (d) with that of the calculated EDPs. This is an example of an experimental image that requires a complete set of EDPs to evaluate all the potential structural possibilities and emphasizes the need for calculating such a set.

These results show that the structures generated from the F-TMT agree with the experimental facts, but before embracing the interpretation of the new images some comments are in order with regard to the modulation contrasts alluded to above. The first one relates to the visibility of the modulation contrasts. According to the set of simulated images included in Fig. 9 the contribution of the superlattice reflections to the image are greatly influenced both by the diffraction and the imaging processes, as should be expected. However, even for very thin crystals these modulations can be imaged under appropriate focusing conditions. Thus, Fig. 10(a) and (d) indicate that even in the DDPs of images for which no modulation is visible by a naked-eye inspection, the superlattice spots can still be detected. It also seems that these reflections that result from the low-frequency contrast modulation maintain a significant intensity on a wider range of focusing conditions for thicker crystals, at least in the thickness range considered here.

The comparison of the calculated images projected along $\langle\bar{1}\ 1\ 0\rangle_F$ shown in Fig. 9 with the [0 1 0] projection of the structure of the β(1) phase, Fig. 13, indicates that the modulations observed in these images are intimately related to the arrangement of oxygen vacancies. A similar conclusion can be reached from a comparative analysis of the calculated images and structure for other orientations of this phase, Figs. 12 and 13. Note how for specific defocus and thickness values, (Fig. 12(i)–(k)), the contrast modulations which are visible as high intensity points, correlate quite well with the distribution of oxygen vacancies in the oxide. Although such a correlation is not so evident for the rest of calculated images, the DDPs which can be obtained from them still contain information about the superstructure which would allow identification of the phase.

Finally, the interpretation of a complex HREM image shown as Fig. 14(a) will be presented. This figure exemplifies a situation commonly encountered in materials involving reduced rare earth oxide phases, namely the existence of contiguous microdomains with different structures and/or compositions. In this particular image three microdomains, marked A, B and C, can be differentiated simply by inspection of the image. Even the domain

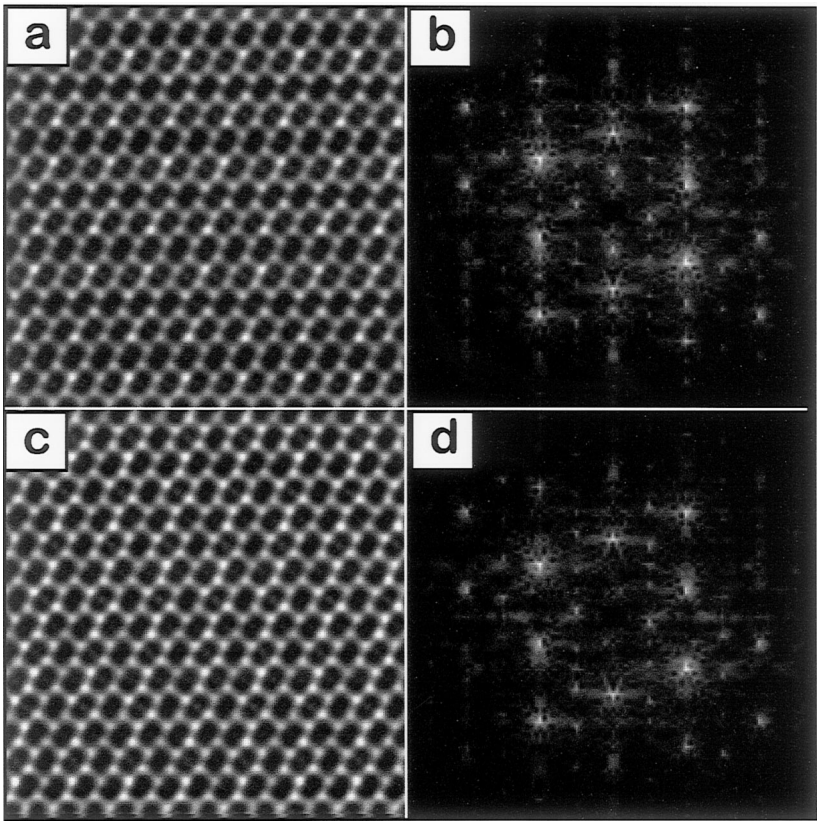

Fig. 11. Simulated images and DDPs of $\beta(3)$-phase (a and b), and ε-phase (c and d).

boundaries can be outlined simply by eye. The DDPs of all three of these domains, Fig. 14(b)–(d), show a common $\langle 1\,1\,0\rangle_{\mathrm{F}}$ substructure with the same orientation. This suggests strongly or even conclusively that they have nucleated and grown within the same parent crystal.

The analysis of the superlattice structure of the DDP corresponding to the region labeled as A, Fig. 14(b), indicates that this region could correspond to a domain of $\beta(3)$ phase in $[6\,\bar{1}\,0]$ orientation. The calculated EDP for $[6\,\bar{1}\,0]_{\beta(3)}$, Fig. 4(g), is characterized by the presence of three superstructure spots along the $[\bar{1}\,1\,1]_{\mathrm{F}}$ direction, which is exactly the feature observed in the experimental DDP. The calculated image, shown as an inset in Fig. 15, for a crystal of $\beta(3)$ 20 nm thick along $[6\,\bar{1}\,0]_{\beta(3)}$ satisfactorily reproduces the contrasts observed in the experimental recording of this region, hence, supports the proposed interpretation. The calculated EDP for the $[3\,\bar{1}\,0]$ zone axis of $\beta(1)$, Fig. 4(c), also contains three superlattice spots along $[\bar{1}\,1\,1]_{\mathrm{F}}$, but dynamic calculations indicate that just the one at the center has a significant intensity, whereas, those at $\frac{1}{4}$th and $\frac{3}{4}$th are extremely weak. Thus the assignment of the experimental image to $[3\,\bar{1}\,0]_{\beta(1)}$ does not seem very likely. In effect, the calculated images obtained for this phase and orientation do not match the experimental contrasts very well, Fig. 16(a). The DDP corresponding to this calculation contains only a very intense central spot but fails to reproduce those at $\frac{1}{4}$th and $\frac{3}{4}$th observed in the experimental DDP.

The DDPs of regions of small dimensions in the area marked B, Fig. 14(e), are similar to those shown previously in Fig. 8. It seems reasonable

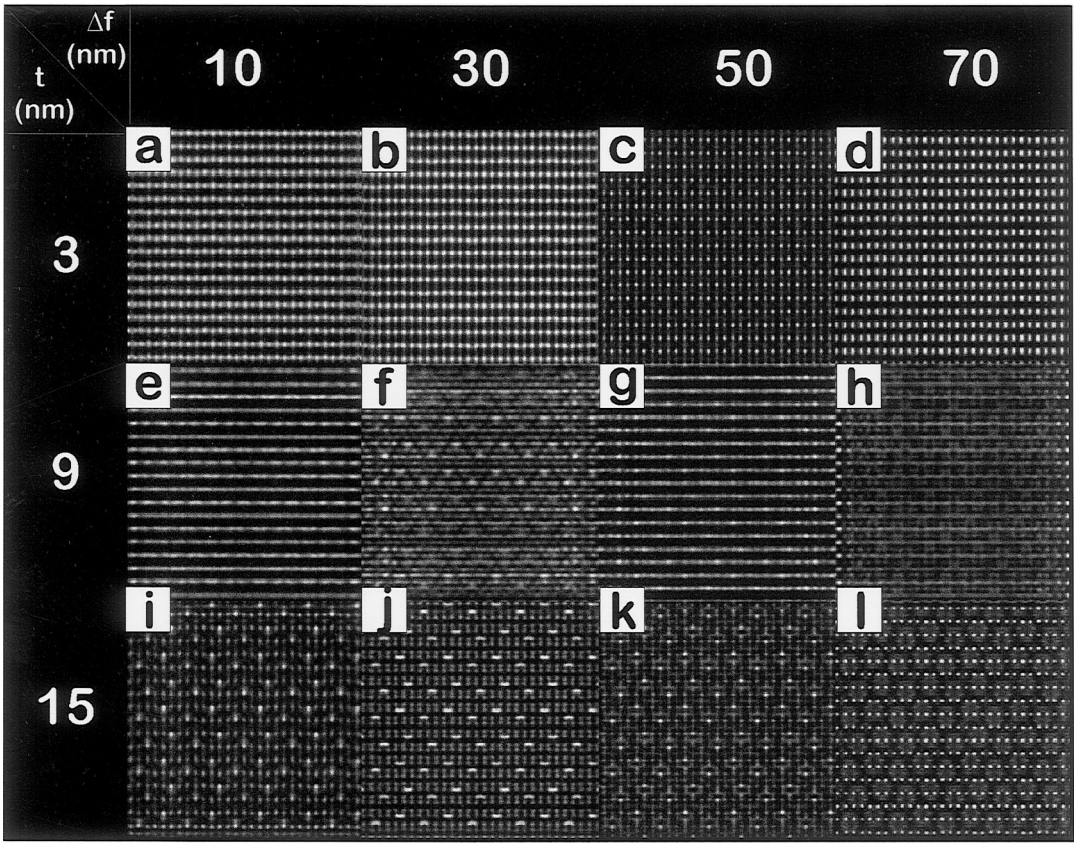

Fig. 12. Simulated images for the $[1\,1\,2]_F$ zone of $\beta(1)$-phase according to thickness and defocus.

therefore, to assign this zone of the micrograph to $[0\,1\,0]_{\beta(1)}$. The dark band contrasts characteristic of this orientation of $\beta(1)$, as depicted in the calculated image of Fig. 9(j), are clearly observed in this region of the crystal. If the image is viewed in glancing angle, it can be observed that these dark bands do not extend across the whole, presumably $\beta(1)$, region. Instead they have a limited extension and shift aside from one region of the image to another in a complex fashion. This shift effect gives rise to the appearance of satellites close to the main superlattice spots, in DDPs obtained from large areas of this region, like that in Fig. 14(d). In any case, these satellites cannot be assigned to additional superlattice spots. This effect may indicate a variation of the vacant oxygen positions in this region.

Finally, the third domain, whose image has been enlarged in Fig. 17, is apparently a region of zeta phase in the $[1\,\bar{1}\,1]_\zeta$ orientation. For this phase and orientation the EDP is characterized by two superlattice spots along $[2\,\bar{2}\,0]_F$, Fig. 4(o). The DDP obtained in this region, Fig. 17(b), clearly indicates the presence of these superlattice spots and matches quite well with those obtained for the calculated images, Fig. 17(c). Given that none of the $[1\,1\,0]_F$-type patterns of any reduced phase contains this particular feature it may be concluded that this assignment is very reliable. In contrast with the other domains, which corresponded to two different polymorphs of the same chemical composition ($PrO_{1.833}$), the reduction state of the praseodymium oxide in this zeta region is higher, $PrO_{1.778}$, which indicates the establishment of an oxygen

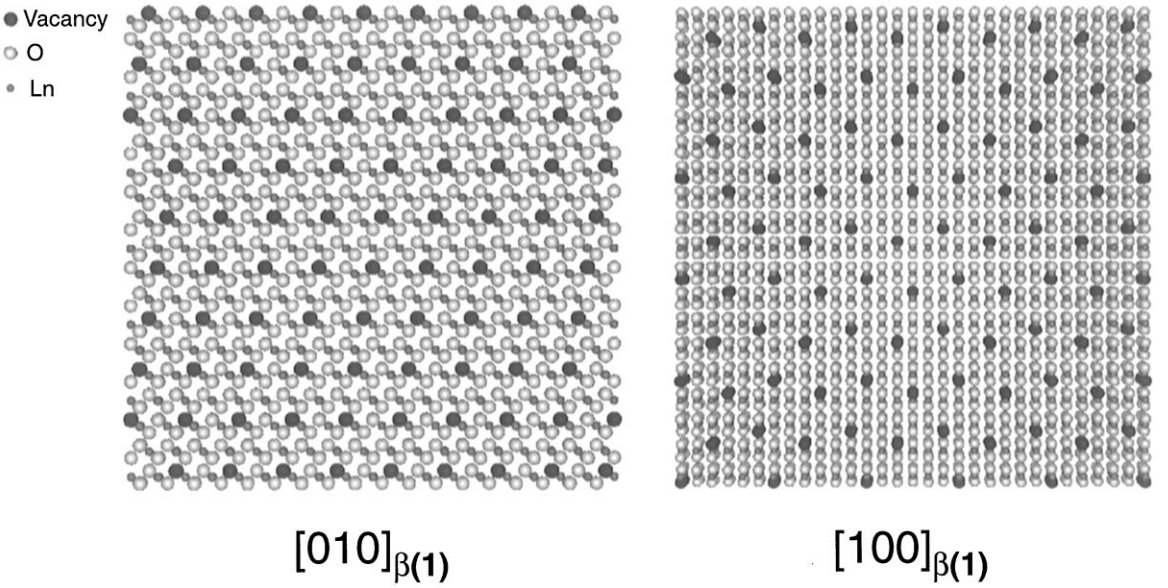

Fig. 13. Projection of the structure of β(1)-phase in two zones.

vacancy gradient within the region. The irregular modulation contrast in the neighboring domain may indicate the variety of vacant oxygen sites. This heterogeneity is not unexpected since the annealed sample was quenched from the non-stoichiometric α-phase of composition $PrO_{1.8}$.

4. Conclusions

The last example illustrates the difficulties inherent in the structural characterization of samples containing rare earth reduced oxides, and the power of electron microscopy techniques to elucidate these complicated situations. Macroscopic techniques may be insensitive to the existence of a mosaic of small microdomains with different crystallography and/ or chemical composition. Nevertheless, the examples presented in this paper clearly demonstrate the capacity of HREM and ED techniques to deal with these complexities. The basic information provided by the atlas of calculated EDPs built from the F-TMT recently proposed for the homologous series of reduced rare earth oxides, appears as a requirement to successfully interpret the complexities revealed in HREM studies.

By comparing the superlattice features observed in the calculated patterns included in the atlas developed in this work a set of phase/zone-axis assignments, compatible with experimental EDPs or DDPs can be found. This set may contain only one element, in which case no additional work is required to define the nature of the phase giving rise to the diffraction pattern or image. Further simulation work would be focused in that case to get a deeper insight into the complementary structure details. In those cases where more than one phase/zone axis is included in the set, further dynamic calculations and/or image simulations would be required to reduce this primary set to a unique, definite solution. This strategy has been applied and discussed in detail for particular cases.

Finally, it is of utmost importance to emphasize that the success obtained in the interpretation of the experimental facts presented here, provides additional support to the model recently established for this family of phases.

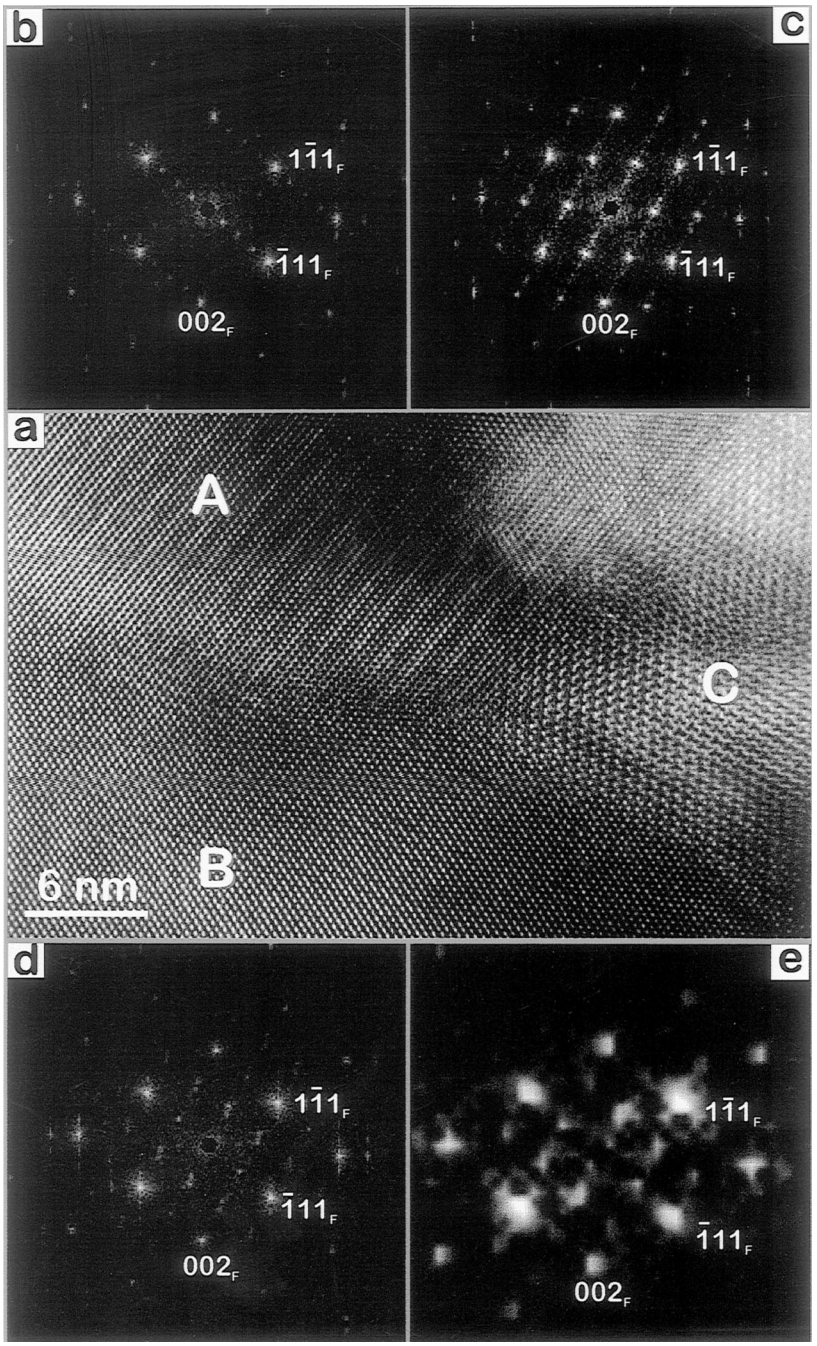

Fig. 14. Experimental image of a quenched a-phase, PrO_x, with DDPs of the regions A and (b) for $\beta(3)$-phase, B and (d) for $\beta(1)$-phase, and C and (c) for ζ-phase.

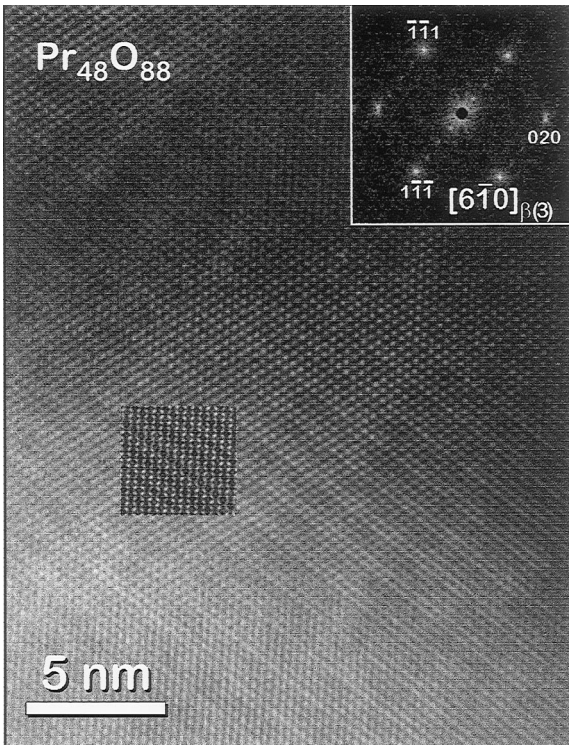

Fig. 15. Experimental image of $\beta(3)$-phase, with image simulation and DDP insets.

Acknowledgements

This work has received financial support from CICYT (Proj. Ref.: MAT96-0931), CICYT (Proj. Ref.: PB95-1257) and the Junta de Andalucía. Experimental HREM images were obtained at ASU. Arizona State University provided the salary for Z.C.K.

References

[1] L. Eyring, in: K.A. Gschneidner Jr, L. Eyring (Eds.), Handbook on the Physics and Chemistry of the Rare Earths, Vol.3, Amsterdam, North-Holland, 1979, p. 337, Chapter 27.
[2] R.G. Haire, L. Eyring, in: K.A. Gschneidner Jr, L. Eyring (Eds.), Handbook on the Physics and Chemistry of the Rare Earths, Vol. 18, Amsterdam, North-Holland, 1994, p. 413, Chapter 125.
[3] S. Bernal, G. Blanco, M.A. Cauqui, P. Corchado, J.M. Pintado, J. M. Rodriguez-Izquierdo, H. Vidal, Stud. Surf. Sci. and Catal. 116 (1998) 611.
[4] S. Bernal, G. Blanco, G. Cifredo, J.A. Perez-Omil, J.M. Pintado, J.M. Rodriguez-Izquierdo, J. Alloys Compounds 250 (1997) 449.
[5] P. Fornasiero, J. Kaspar, M.J. Graziani, J. Catal. 167 (1997) 576.
[6] P. Kunzmann, L. Eyring, J. Solid State Chem. 14 (1975) 229.
[7] R.T. Tuenge, L. Eyring, J. Solid State Chem. 41 (1982) 75.

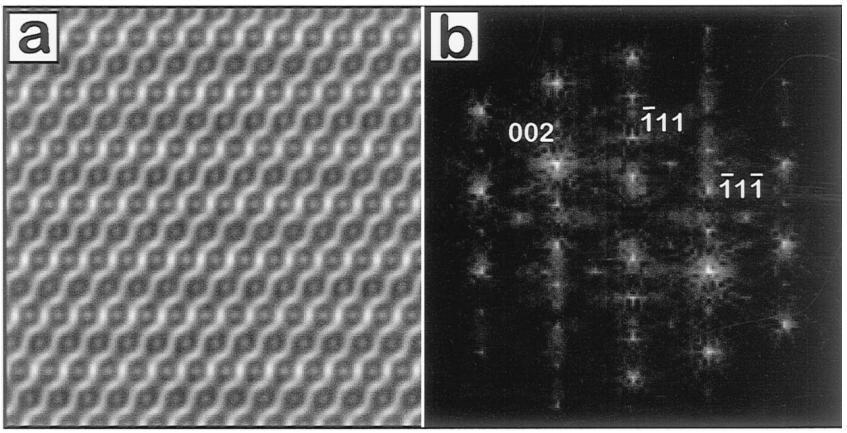

Fig. 16. Simulated image and DDP of $\beta(1)$-phase.

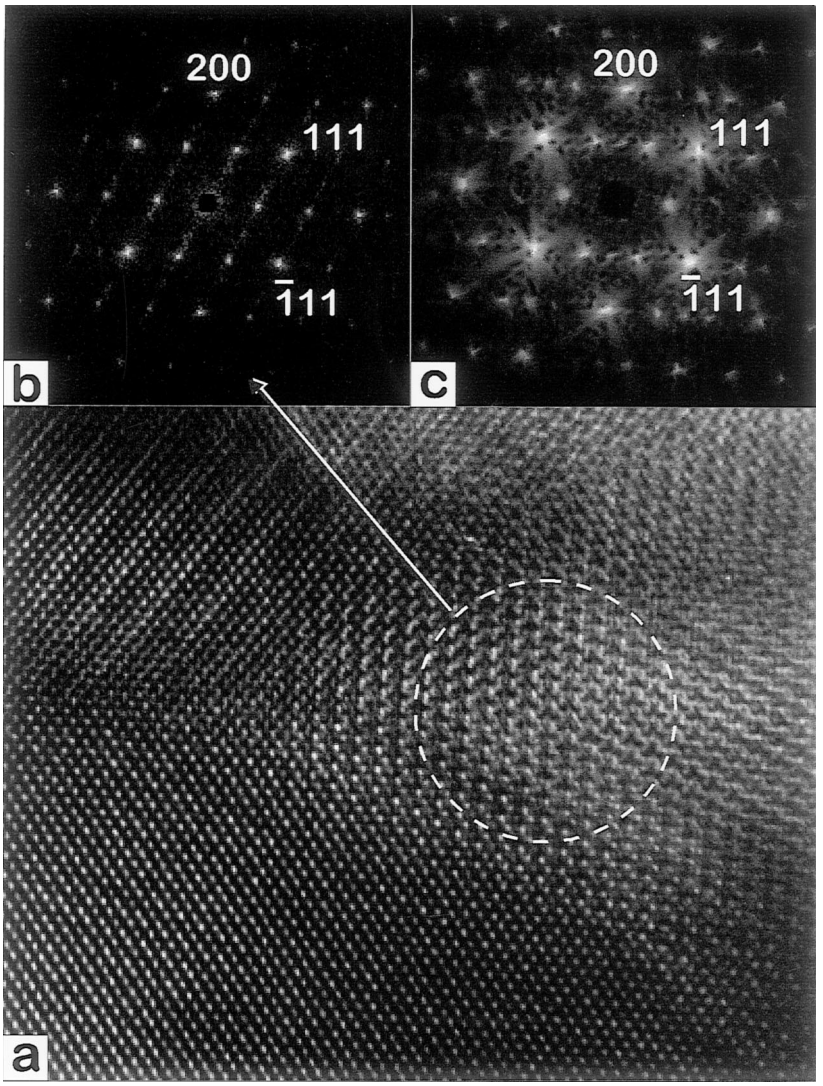

Fig. 17. Experimental image of region C of Fig. 14 with the experimental DDP (b) and the calculated EDP (c) of the $[0\ \bar{1}\ 1]_F$ zone of ζ-phase.

[8] E. Summerville, R.T. Tuenge, L. Eyring, J. Solid State Chem. 24 (1978) 21.
[9] E. Schweda, L. Eyring, J. Solid State Chem. 78 (1989) 1.
[10] E. Schweda, L. Eyring, Ultramicroscopy 23 (1987) 443.
[11] E. Schweda, D.J.M. Bevan, L. Eyring, J. Solid State Chem. 90 (1991) 109.
[12] J. Zhang, R.B. Von Dreele, L. Eyring, J. Solid State Chem. 104 (1993) 21.
[13] J. Zhang, R.B. Von Dreele, L. Eyring, J. Solid State Chem. 118 (1995) 133.
[14] J. Zhang, R.B. Von Dreele, L. Eyring, J. Solid State Chem. 118 (1995) 141.
[15] J. Zhang, R.B. Von Dreele, L. Eyring, J. Solid State Chem. 122 (1995) 53.
[16] Z.C. Kang, L. Eyring, Aust. J. Chem. 49 (1997) 981.
[17] Z.C. Kang, J. Zhang, L. Eyring, Z. Anorg, Allg. Chem. 622 (1996) 465.
[18] Z.C. Kang, L. Eyring, J. Alloys Compounds 249/250 (1997) 206.

[19] Z.C. Kang, L. Eyring, J. Alloys Compounds 275–277 (1998) 30.
[20] Z.C. Kang, L. Eyring, Dalton Transactions of the Royal Chemical Society, submitted for publication.
[21] F.J. Botana, J.J. Calvino, G. Blanco, M. Marcos, J.A. Perez-Omil, Electron Micros. 2B (1994) 1085.
[22] Z.C. Kang, J. Zhang, L. Eyring, Aust. J. Chem 45 (1992) 1499.
[23] P. Stadelmann, Ultramicroscopy 21 (1987) 131.
[24] Z.L. Wang, Z.C. Kang, Functional and Smart Materials, Plenum Press, New York, 1998, pp. 367ff.